Yao, Penghui; Zhang, Jian; Qiu, Qianyuan; Zhao, Yicheng; Yu, Fangyong; Li, Yongdan

A dual modification strategy of highly active catalytic cathode for proton-conducting solid oxide fuel cell with Ni-doped PrBaFe$_{1.9}$Mo$_{0.1}$O$_{6-\delta}$

A dual modification strategy of highly active catalytic cathode for proton-conducting solid oxide fuel cell with Ni-doped PrBaFe$_{1.9}$Mo$_{0.1}$O$_{6-\delta}$

Penghui Yao [a], Jian Zhang [b], Qianyuan Qiu [a], Yicheng Zhao [b], Fangyong Yu [a,c], Yongdan Li [a,*]

[a] Department of Chemical and Metallurgical Engineering, Aalto University, Kemistintie 1, FI-00076, Aalto, Finland
[b] Collaborative Innovation Center of Chemical Science and Engineering (Tianjin), Tianjin Key Laboratory of Applied Catalysis Science and Technology, State Key Laboratory of Chemical Engineering (Tianjin University), School of Chemical Engineering and Technology, Tianjin University, Tianjin, 300072, China
[c] School of Chemistry and Chemical Engineering, Shandong University of Technology, Zibo, 255049, China

HIGHLIGHTS

- PBFMN cathode exhibits excellent ORR and proton transfer rates.
- NiO nanoparticles enhance oxygen adsorption and dissociation.
- Power density of 1.23 W cm^{-2} is measured at 700 °C.
- The triple-conductive mechanism of PBFMN is investigated.
- The dual effect in both perovskite phase and NiO nanoparticles promotes cathode.

GRAPHICAL ABSTRACT
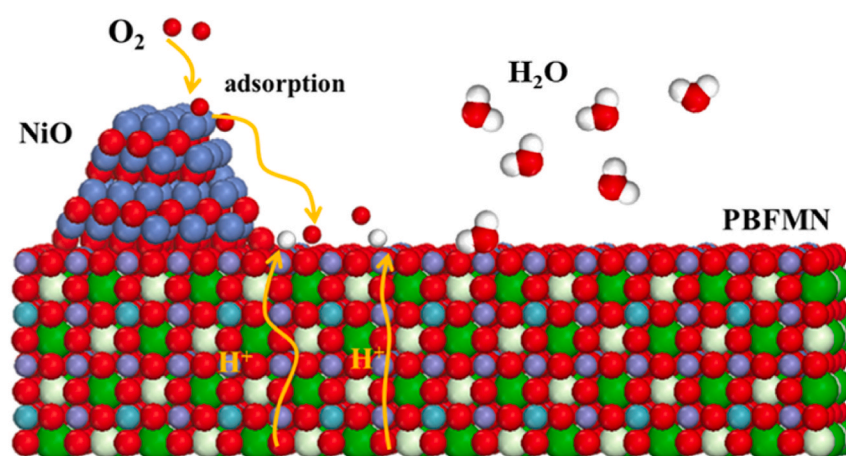
ARTICLE INFO

ABSTRACT

The cathode catalytic activity and stability in a temperature range of 550–700 °C is crucial to the development of proton-conductive solid oxide fuel cells (PCFCs). A facile dual-modification strategy is developed for the design of Ni-doped PrBaFe$_{1.9}$Mo$_{0.1}$O$_{6-\delta}$ (PBFMN), composed of a major perovskite and a minor NiO phases, as a cobalt-free cathode. The composite cathode PBFMN exhibits high catalytic activity and stability. Computational simulation indicates that the perovskite phase increases the oxygen vacancies and enhances the proton transfer, while nickel oxide nanoparticles improve oxygen adsorption and dissociation. The fuel cell with as-prepared PBFMN reached a peak power density 1.23 W cm^{-2} at 700 °C. The improved performance of the cell is mainly due to the fast ORR kinetics. This work provides a new insight into the design of cobalt-free cathode for a PCFC.

1. Introduction

With the growing energy demands, much attention has been devoted to find clean and efficient energy transformation devices [1,2]. Solid oxide fuel cells (SOFCs) are one of the most promising candidates. Conventional SOFCs with the oxygen ion-conducting electrolyte operate at high temperatures (700–800 °C), limiting their broad utilization [3, 4]. Proton-conductive solid oxide fuel cell (PCFCs) have emerged as an energy conversion device in the pursuit of efficient and clean energy conversion [5]. Their ability to operate at reduced temperatures, typically within a range of 550–700 °C, offers a compelling solution to the challenges of conventional SOFCs [6,7]. Moreover, H_2O is produced on the cathode, avoiding the dilution of the fuels and improving fuel utilization efficiency [8]. However, the sluggish oxygen reduction reaction (ORR) kinetics and proton transfer rate on the cathode impedes their practical applications [9,10].

Many triple conducting oxides ($H^+/e^-/O^{2-}$) have been reported as the cathode materials for PCFCs, such as $Ba_{0.5}Sr_{0.4}Co_{0.6}Fe_{0.4}O_{3-\delta}$ (BSCF) [11,12], $PrCo_{0.7}Ni_{0.3}O_{3-\delta}$ [13], and $PrBa_{0.5}Sr_{0.5}Co_{1.5}Fe_{0.5}O_{5+\delta}$ (PBSCF) [14]. These cobalt-containing cathodes have been demonstrated to be efficient to improve ORR activity and the proton conductivity in PCFCs. For example, BSCF as a cathode shows the maximum power density (P_{max}) of 829 mW cm^{-2} at 650 °C. Bi and his co-workers [15] doped BSCF with Mo to improve the protonation ability. The peak power density of a cell increases from 904 to 1217 mW cm^{-2} after doping Mo. Although cobalt-containing cathode exhibits relatively high catalytic activity and performance, their poor chemical stability and mismatch in thermal expansion remain as challenges [16,17]. $PrBaFe_2O_{5+\delta}$ is often used as an anode and cathode in traditional SOFCs due to its low thermal expansion coefficient [3,7,18]. Zhou et al. [19] developed $(PrBa)_{0.95}(Fe_{0.9}Mo_{0.1})2O_{5+\delta}$ cathode for a SOFC. The interfacial polarization of $(PrBa)_{0.95}(Fe_{0.9}Mo_{0.1})2O_{5+\delta}$ is lower than $PrBaFe_2O_{5+\delta}$ in SOFC. Joo et al. [20] used $PrBaFe_2O_{5+\delta}$ as the symmetrical electrode in a PCFC. The P_{max} of a cell with PBFM reached 301 mW cm^{-2} at 700 °C.

Recently, surface modification techniques have been intensively adopted to improve catalytic activity and stability in PCFCs [21]. For example, Zhang et al. [22] infiltrated $Pr_{0.9}Fe_{0.7}Co_{0.3}O_3$ into PBSCF cathode to improve ORR activity and durability. Jing et al. [23] successfully designed $Ba_{0.95}La_{0.05}Fe_{0.8}Zn_{0.2}O_{3-\delta}$-infiltrated $BaCe_{0.7}Zr_{0.1}Y_{0.1}Yb_{0.1}O_{3-\delta}$ cathode, which increased the proton-accessible cathode area at the cathode/electrolyte interface. However, the weak contact between different phases results in lower catalytic activity and poor stability [24,25]. The selective exsolution technique is also an effective way to enhance the electrocatalytic activity, especially in the anode for SOFCs [26,27]. For example, our group developed Sn nanoparticles modified $Ce_{0.70}Sn_{0.10}Sm_{0.2}O_{2-\delta}$, which improved the coking resistance of the anode of a SOFC [28]. Moreover, we developed a Co–Fe doped $La_{0.5}Ba_{0.5}MnO_{3-\delta}$ anode with a unique cubic-hexagonal phase and core-shell nanoparticles, which shows excellent performance and resistance to carbon buildup in SOFCs [29]. However, the application is predominantly utilized in anodes or cathode materials containing cobalt, with limited research effort paid on cobalt-free cathodes.

In this work, $PrBaFe_{1.7}Mo_{0.1}Ni_{0.2}O_{6-\delta}$ (PBFMN) is designed as a cobalt-free cathode in a PCFC with fast ORR kinetics and proton transfer. PBFMN consists of a major Ni-doped PBFM perovskite phase and formed NiO nanoparticles. The effects of Ni in both perovskite and the second phases NiO are investigated. We investigate the ORR activity and stability of PBFMN modified with nickel oxide nanoparticles in PCFCs through a combination of experiment and theoretical analysis. Compared to PBFM, the PBFMN exhibits higher oxygen vacancy concentration and faster proton transfer. The PBFMN cathodes delivers a peak power density 1.23 W cm^{-2} in a PCFC with the $BaZr_{0.1}Ce_{0.7}Y_{0.2}O_{3-\delta}$ (BZCY) electrolyte at 700 °C, and a good stability without obvious degradation in 200 h.

2. Materials and methods

2.1. Preparation of cathode powders

$PrBaFe_{1.9}Mo_{0.1}O_{6-\delta}$ (PBFM) and $PrBaFe_{1.7}Mo_{0.1}Ni_{0.2}O_{6-\delta}$ (PBFMN) were synthesized with a sol-gel technique. 20 mol.% Ni is partially substitute for Fe site of PMFM to form PBFMN. Stoichiometric amounts of $Pr(NO_3)_3 \cdot 6H_2O$, $Ba(NO_3)_2$, $Fe(NO_3)_3 \cdot 9H_2O$, $(NH_4)_6Mo_7O_{24}$ and Ni $(NO_3)_2 \cdot 6H_2O$ were dissolved in deionized water. Ethylenediaminetetraacetic (EDTA, 99.5 %) and citric acid was then added to the solution. Afterwards, the pH value of the solution was adjusted to 7.5 with addition of ammonia solution. The obtained solution was stirred until it changed to a gel and then heated at 300 °C. The precursor was calcined at 950 °C for 3 h.

2.2. Fabrication of the fuel cell and test

The electrolyte $BaZr_{0.1}Ce_{0.7}Y_{0.2}O_{3-\delta}$ (BZCY) powder was synthesized with a sol-gel technique [30]. The anode consisted of 70 wt% electrolyte, 30 wt% NiO and 10 wt% starch. The mixture was pressed into 15 mm diameter pellet and calcined at 1100 °C for 2 h to form anode support. An anode functional layer subsequently was spin-coated onto the anode to reduce the thermal expansion mismatch between the electrolyte and the anode. The anode functional layer slurry was prepared with mixing electrolyte and NiO in terpineol with ethyl cellulose. BZCY electrolyte layer was also prepared with spin-coating technique. The electrolyte slurry is composed of electrolyte, terpineol and ethyl cellulose. After coating, the pellet was co-calcinated at 1400 °C for 3 h [31,32]. The prepared cathode material was mixed with V006 binder to get a cathode slurry. The cathode slurry was casted on the electrolyte side with a screen-printing method. Finally, the sample was sintered at 950 °C for 3 h to obtain the single cell.

The I–V and I–P curves of the cells were recorded using an electrochemical workstation VERSASTAT 3 under H_2 as fuels and oxygen as oxidant. The polarization of the cathode was measured with a symmetric cell. The electrolyte disk was prepared with pressing the BZCY at 500 MPa and sintering at 1350 °C for 5 h. The symmetric cell was obtained with casting cathode slurry onto both sides of the electrolyte disk.

2.3. Characterization

The x-ray diffraction (XRD) pattern was measured with a PANalytical X'PertPro diffractometer in the 2θ range of 20°–80°. The micromorphology of the materials was observed with a scanning electron microscope (SEM, S-4800, Hitachi). TEM and EDX mappings were recorded with JEOL JEM-2200FS. The X-ray photoelectron spectroscopy (XPS) analysis was performed with an Escalab 250Xi system with an Al-Kα radiation.

2.4. First principal calculations

All density functional theory (DFT) simulations were performed with the Hubbard-U framework (DFT + U) using the Vienna ab initio simulation package. The values of Ueff = 6.7, 3.8 and 5.2 were employed for Ni, Mn and Fe. Monkhorst–Pack K-point grid was made to 3 × 3 × 3 and 3 × 3 × 1 during bulk and surface relaxation respectively. The plane-wave cut-off energy was applied at 500 eV. The convergence criteria for energy and force were 10^{-5} eV and 0.02 eV/Å, respectively. The oxygen vacancy formation energy (E_{vo}) of the PBFM and PBFMN are obtained using the following equation,

$$E_{vo} = E_{defect} + \frac{1}{2}E_{O_2} - E_{perfect} \tag{1}$$

E_{defect} represents the energy of the bulk with a single oxygen vacancy, while E_{O_2} denotes the energy of an oxygen molecule. $E_{perfect}$ signifies the energy of the stoichiometric bulk [11,15].

The hydration energy (E_h) was computed using the following equation,

$$E_h = E_{2OH} - E_{H_2O} - E_{defect} \qquad (2)$$

Where E_{2OH} represents the bulk energy with two protons, E_{H_2O} is the energy of a water molecule, and E_{defect} is the energy of bulk with a single oxygen vacancy [24,33].

The oxygen adsorption energy (E_{ad}) was defined as

$$E_{ad} = E_{tot} - E_{slab} - E_{O_2} \qquad (3)$$

E_{tot} represents the energy of the adsorption surface, E_{slab} is the cathode surface energy, and E_{O_2} is O_2 molecule energy.

3. Results

3.1. Electrochemical performance

The SEM images of the prepared fuel cell, as depicted in Fig. 1a, illustrates a highly dense electrolyte layer with a thickness of approximately 25 μm. Fig. 1b and c shows the I–V and I–P curves of the single cells with PBFM and PBFMN fed with wet H_2 from 550 to 700 °C. The measured open circuit voltages (OCV) of the cells are in the range of 1.00–1.05 V. These values indicate that the electrolyte is dense without any gas leakage, in consistency with the SEM images. The cell with PBFM cathode exhibits a P_{max} 886 mW cm^{-2} at 700 °C. When PBFMN was used as the cathode, the cell shows a P_{max} 1.23 W cm^{-2} at 700 °C. With decreasing the temperature, the P_{max} of the cell with PBFMN as cathode drops to 897, 795, 626 mW cm^{-2} at 650, 600, 550 °C, respectively. The performance is one of the best of the reported values for cobalt-free cathodes in PCFCs (Fig. 1d) [7,34–38]. The corresponding EIS curves of single cells measured at 700, 650 and 600 °C are presented in Fig. 1e. The ohmic resistances of both cathodes are similar. Remarkably, the polarization resistance of PBFMN is significantly lower than that of PBFM. To gain insights into the polarization processes, DRT analysis is subsequently carried out and presented in Fig. 1f and g. Five peaks are labeled P1–P5 from low to high frequency. Previous studies reported a correspondence between DRT peaks and electrode reactions [35,39,40]. P1 represents adsorption and dissociation of oxygen at the cathode. P2 presents is associated with proton transfer at the cathode. P3 represents the oxygen incorporation from surface to bulk at the cathode. P4 and P5 are assigned to proton diffusion and hydrogen adsorption at the anode. It is obvious that the P1 and P2 peaks decrease the most. This means that the introduction of Ni is mainly beneficial to the adsorption and dissociation of oxygen and the migration of protons. In PBFM, the cathode processes are rate-limiting steps, which accounts for most of the polarization. After Nimost doping, the cathode polarization is reduced, and the anode processes are the rate-limiting steps. Additionally, the stability test is carried out for 200 h at 700 °C under a current density of 1 A/cm^2 (Fig. 1e). The degradation rate is estimated as 0.04 V/kh.

Fig. 2a illustrates the EIS curves of symmetrical cells with PBFM and PBFMN cathodes, tested in oxygen at 700 °C and 650 °C. The polarization resistance (R_P) is reflected by intersection point with the end of the X axis. R_P of PBFMN cathode at 700 °C and 650 °C is approximately 0.05 and 0.14 Ω cm^2, respectively. PBFM exhibits R_P values of 0.17 and 0.45 Ω cm^2 at 700 °C and 650 °C respectively. Fig. 2b present Arrhenius plots of R_P for the symmetric cells. For both cathodes, R_P decreases with increasing temperature. The slopes for PBFMN are smaller than those for PBFM. The slopes correspond to activation energies (E_a), where PBFMN exhibits an E_a of 1.33 eV, which are lower than PBFM's E_a of 1.35 eV. The E_a of PBFM also decreases after the Ni doping. The low activation energy of PBFMN indicates low ORR barrier.

To investigate the cathode ORR activity, the distribution of relaxation time (DRT) of the symmetrical cell is used to analyze impedance responses. The DRT curves are further subdivided into the low-frequency intersection P1, the intermediate-intersection P2 and the high-frequency

P3. DRT of PBFMN under different partial pressure of O_2 was analyzed (Fig. 2c). At the same temperature, as the oxygen partial pressure increases, the low-frequency part remains essentially unchanged. The intermediate-frequency part is the most dependent on the concentration of oxygen. The polarization resistance (R_P) of each process is calculated from peak integration areas from DRT plot of P1, P2 and P3 respectively (Fig. 2d). The dependent relationship of R_P on P_{O2} is fitted with $R_P = k$ $(P_{O2})^{-n}$. The P1 shows a weaker P_{O2} dependence, indicating that P1 is related to the oxygen ion transport across the electrolyte/electrode interface. n = 0.301 for P2 suggests that the rate-determining step of the P2 is the reduction of oxygen atoms to O^- [41,42]. The n value for P3 is 0.144, indicating that P3 correspond to the charge transfer process. Fig. 2e further compares DRT plots of PBFM and PBFMN. After Ni doping, the resistance of PBFMN cathode in all the frequency intersections decreases remarkably. Compared to those of PBFM, the area of P3 in PBFMN significantly decreased, indicating that PBFMN have higher charge transfer process. The P2 areas of PBFMN are smaller than those of PBFM, suggesting faster oxygen reduction process on PBFMN.

3.2. Characterization

In Fig. 3a and b, the X-ray diffraction (XRD) patterns before and after nickel (Ni) doping to PBFM are presented. The XRD peaks remain at similar locations before and after Ni doping. After nickel doping, the peak intensity is increased, indicating that Ni doping improves crystallinity of PBFM. An additional small peak at 42° is observed, which corresponds to NiO phase. Moreover, Fig. 3b reveals a noticeable shift of the peaks towards lower angles in the XRD pattern of the PBFMN than that of the undoped PBFM, indicating the successful incorporation of nickel into the perovskite (PBFM) lattice. The crystal lattice distortion is ascribed to lower ionic radius of doped Ni atoms than Fe. Rietveld refinement of XRD data for PBFMN is performed with the results shown in Fig. 3c. A cubic perovskite structure (space group Pm-3m) is calculated for PBFMN with parameters to be a = b = c = 3.925 Å. A secondary phase is identified as NiO. The lattice parameter of NiO is a = b = c = 4.177 Å. The result shows that the NiO relative amount is 2.7 wt%. Fig. 3d shows the lattice fringes are 0.241 and 0.283 nm, which are corresponded to the (111) plant of the NiO phases and the (110) plant of perovskite phase, respectively. Transmission electron microscopy (TEM) mapping is employed to investigate the elemental distribution within the doped sample. The mapping results revealed uniform distribution of Pr, Ba, Fe, and Mo in the bulk phase (Fig. 3e). Notably, the mapping of Ni and O displayed the presence of the NiO nanoscale particle on the surface. It is consistent with the analyses of XRD results. The NiO nanoparticles exhibit an average diameter of approximately 100 nm.

The O 1s spectra of PBFM and PBFMN samples are plotted in Fig. 4a. The high-resolution O 1s spectrum consists of adsorbed (O_{ad}), lattice (O_{lat}) oxygen, O_2^{2-}/O^- and adsorbed H_2O [35]. The O_{lat}/O_{ad} peak area ratio of PBFM and PBFMN samples are 0.56 and 0.73 respectively, which represents that more oxygen vacancies are existed in PBFMN. Fig. 4b shows the Fe 2p spectra of PBFM and PBFMN. The results reveal the mixed-valence state of Fe^{3+} (located at 723.2 and 710.1 eV) and Fe^{4+} (located at 725.1 and 711.7 eV). The content of Fe^{3+} increases from 43.46 % to 52.13 % after doping Ni, indicating a decrease of the valence state of Fe after doping Ni. Using Kroger–Vink notation, the defect reaction is presented by:

$$2Fe_{Fe}^{\times} + O_O^{\times} \leftrightarrow 2Fe_{Fe}^{'} + V_O^{\bullet\bullet} + \frac{1}{2}O_2 \qquad (4)$$

Where $Fe_{Fe}^{\times}$ and $Fe_{Fe}^{'}$ denote Fe^{4+} and Fe^{3+} respectively. $O_O^{\times}$ and $V_O^{\bullet\bullet}$ represents lattice oxygen and oxygen vacancy respectively. The value of iron decreases, indicating the loss of some electrons. These lost electrons typically transfer to lattice oxygen, leading to a reduction in the oxygen atoms and consequently forming oxygen vacancies.

In addition, thermogravimetric analysis (TGA) is used to determine
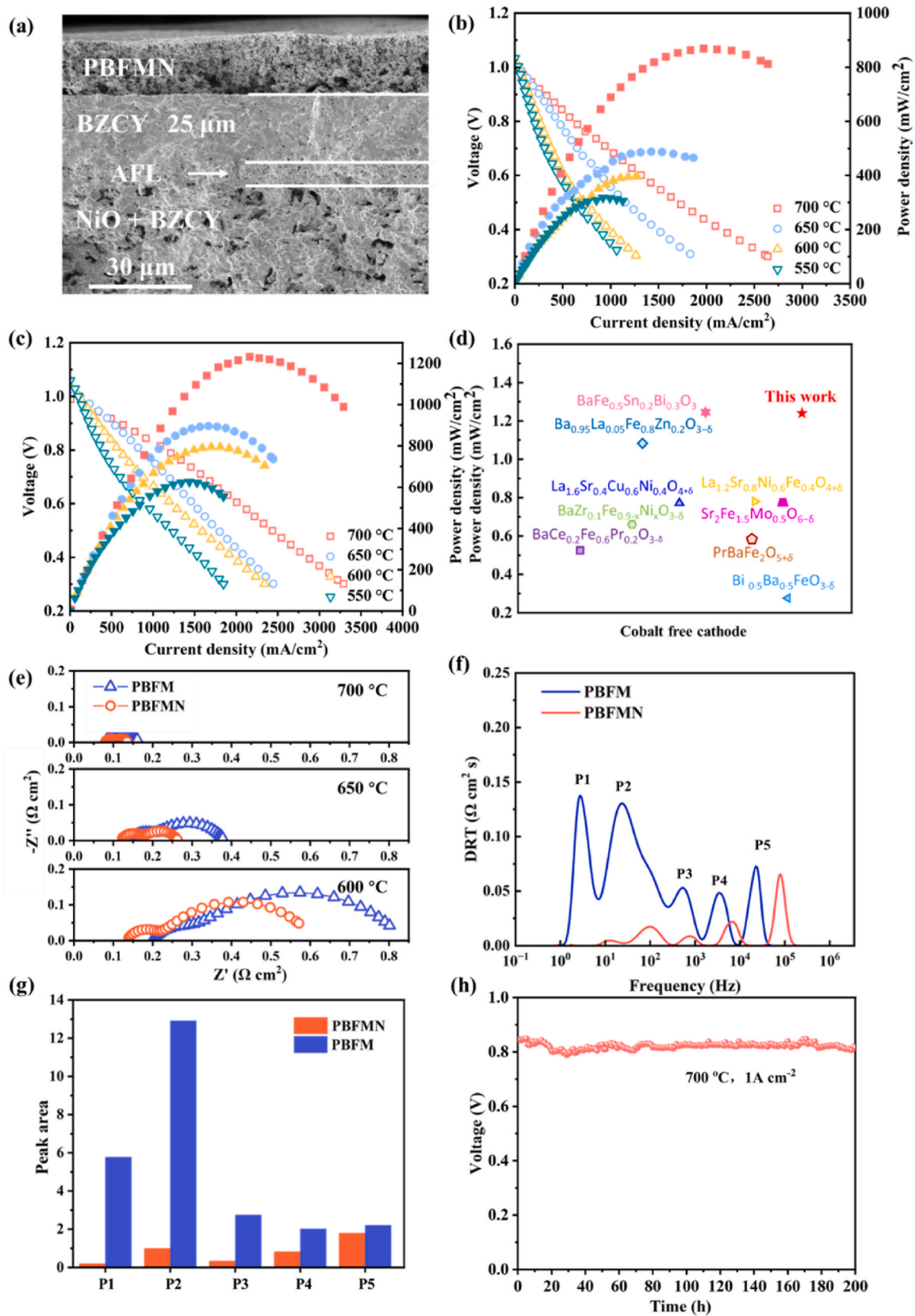
Fig. 1. (a) Cross-sectional SEM image of single cell. (b) I–V and I–P curves of single cells with PBFM cathode. (c) I–V and I–P curves of single cells with PBFMN cathode. (d) Comparison of Pmax of PBFMN (red) with other representative PCFC cobalt-free cathodes at 700 °C. (e) EIS of the single cell with PBFM and PBFMN at 700, 650, 600 °C. (f) DRT curves of PBFM and PBFMN cathodes in single cell at 600 °C. (g) The peak area of each peak. (h) Durability test result of the cell with PBFMN cathode under a constant current density of 1 A cm^{-2} at 700 °C.
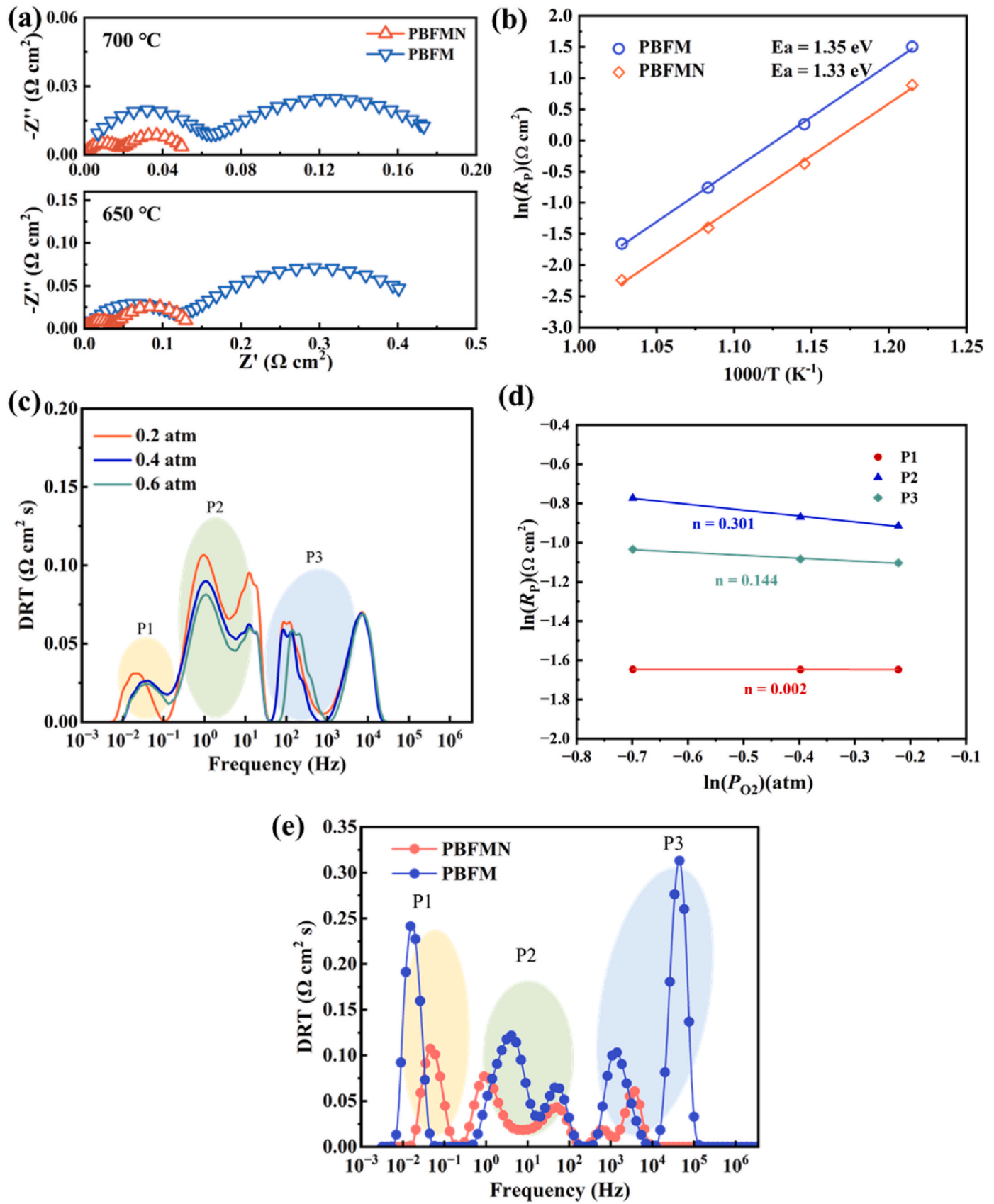
Fig. 2. (a) EIS of symmetric cells with PBFM and PBFMN in O_2 at 700 and 650 °C. (b) R_p of cathodes in O_2 at various temperatures. (c) DRT curves of PBFMN under different oxygen partial pressures. (d) Profile of dependence of P_{O2} on resistance of P1, P2 and P3 for PBFMN. (e) DRT curves of PBFM and PBFMN cathodes in O_2 at 700 °C.
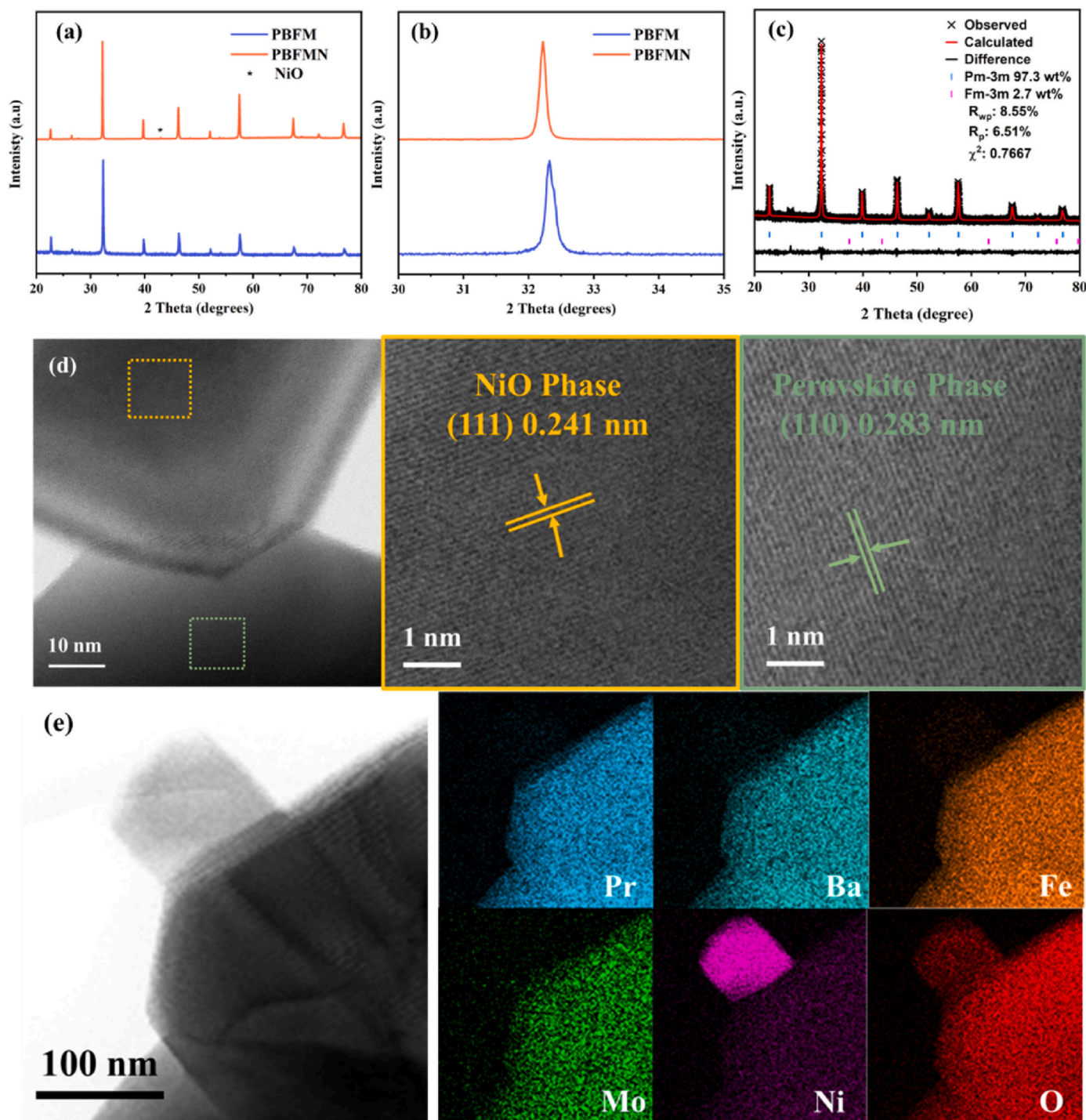
Fig. 3. (a) XRD patterns of the PBFM and PBFMN samples. (b) XRD patterns of the PBFM and PBFMN samples from 30 to 35°. (c) Rietveld refinement profiles of PBFMN. (d)TEM image of the perovskite and NiO phases in PBFMN. (e) TEM micrographs and the corresponding EDS elemental mappings of PBFMN sample.

the lattice oxygen loss of cathode. A slight mass loss below 300 °C is attributed to the desorption of surface adsorbed species. The weight losses begin at 300 °C corresponding to the loss of lattice oxygen. The weight loss of PBFM and PBFMN samples at 700 °C are about 1.48 % and 1.80 % respectively (Fig. 4c).

3.3. Density functional theory simulation

To further understand the ORR and proton transfer mechanism, DFT simulations are carried out. Based on the model of $Pr_4Ba_4Fe_7Mo_1O_{24}$

(PBFM) and $Pr_4Ba_4Fe_6Mo_1Ni_1O_{24}$ (PBFMN), the oxygen vacancy formation energy (E_{vo}), hydration energy (E_h), and proton migration energy barriers are calculated in the different oxygen sites (Fig. 5a and b). The lowest E_{vo} of PBFMN is -0.38 eV, which is much lower than PBFM (0.52 eV). The E_h of PBFMN is -0.878 eV, while the E_h of PBFM is -0.497. The proton transfer includes two steps (hopping and rotation). The simulation results show that the barriers of proton hopping and rotation for PBFMN are both lower than those for PBFM. The hopping energy barrier for PBFMN is 0.045 eV, and for PBFM is 0.268. The rotation energy barrier of PBFM is 0.169 eV, whereas that of PBFMN is
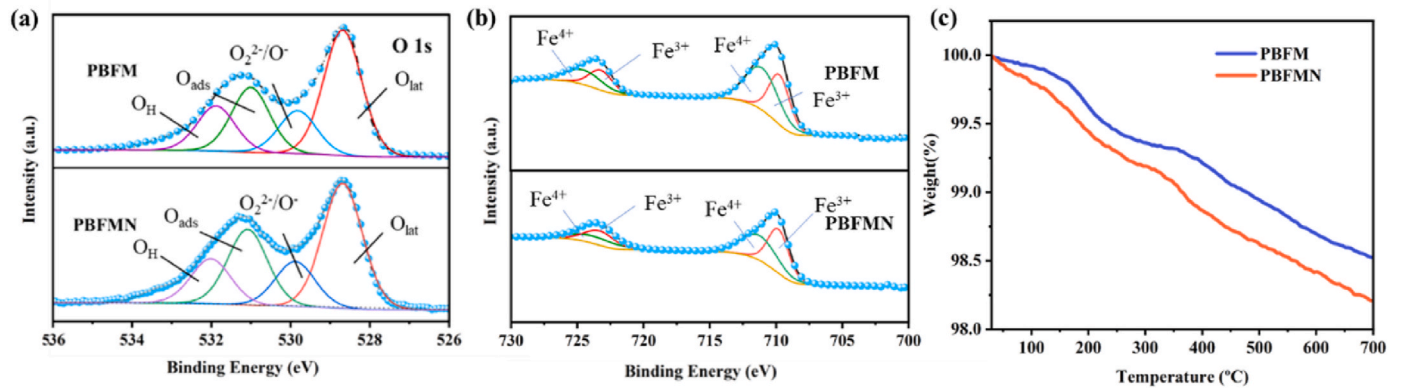
Fig. 4. XPS spectra of (a) O1s and (b) Fe 2p for the PBFM and PBFMN samples. (c) TGA curve of PBFM and PBFMN samples.
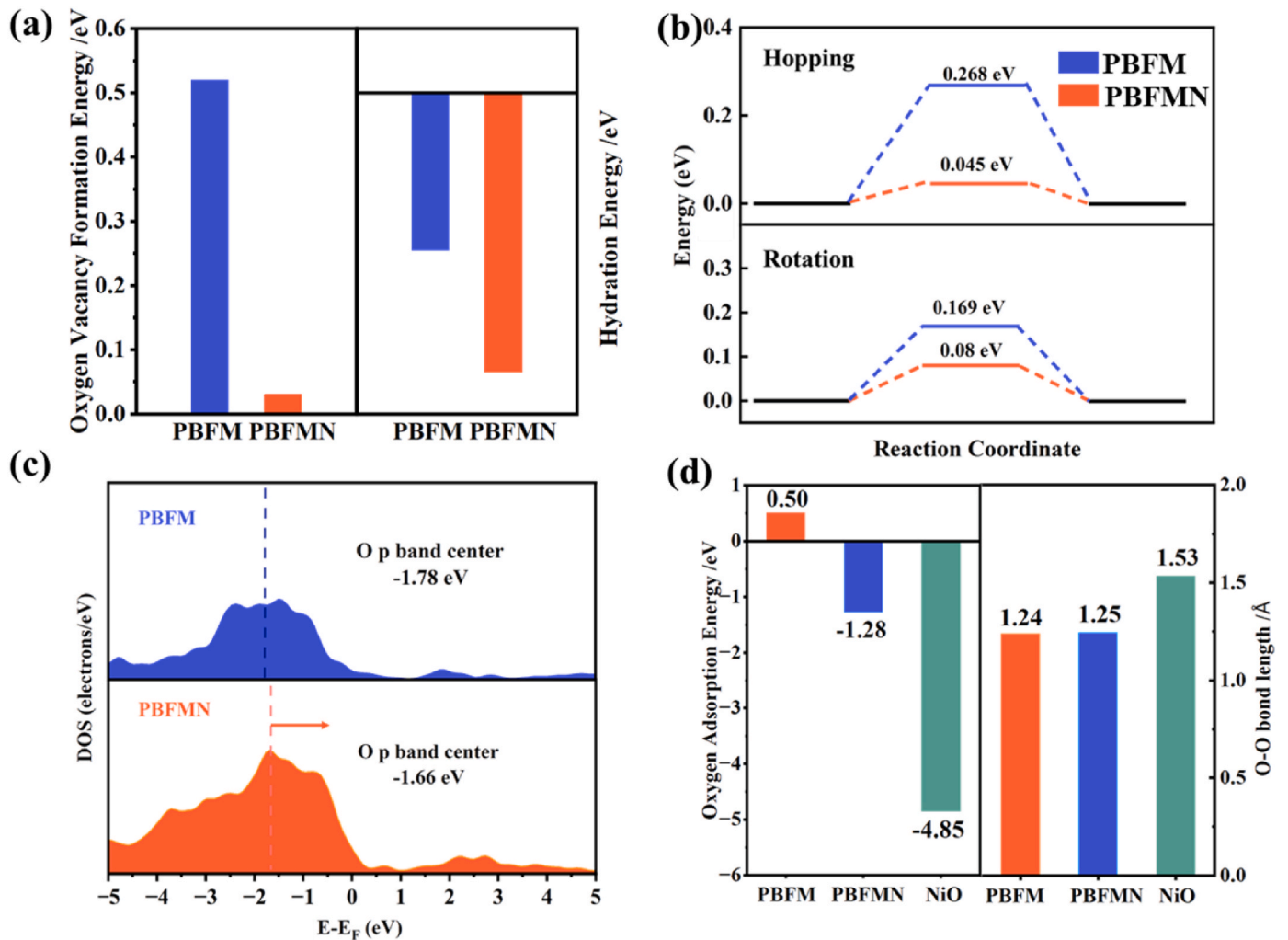

Fig. 5. (a) Oxygen vacancy formation energy and hydration energy of PBFM and PBFMN. (b) Proton migration energy barrier of PBFM and PBFMN. (c) PDOS of O 2p orbitals (spin up and spin down). (d) Oxygen adsorption energy and adsorption O–O bond length of PBFM, PBFMN and NiO.

0.08 eV. The improvement of proton transfer in PBFMN extend the active reaction area to the whole cathode, thus enhancing the cell performance.

Furthermore, the O p-band center is often taken as a descriptor of ORR activity [43]. We calculated the O p-band centers of the two cathodes (Fig. 5c). The O p-band center of PBFMN (-1.22 eV) is higher than that of PBFM (-1.58 eV). We further explored the impact of NiO on

the ORR catalytic activity. The adsorption energy of oxygen on the NiO surface is -4.85 eV. The value is lower than that for PBFM and PBFMN (Fig. 5d). After the oxygen adsorption on the NiO, PBFM and PBFMN surfaces, O–O bond length are compared. The bond length of O–O on the NiO surface is 1.53 Å and that for PBFMN and PBFM are 1.25 and 1.24 Å, respectively. The NiO nanoparticles improve O_2 adsorption and dissociation.

4. Discussion

4.1. ORR activity and proton transfer

ORR activity is closely associated with high triple conductivity (e^-, H^+, and O^{2-}) and surface exchange in the cathode. High oxygen vacancy concentration facilitates the oxygen transfer and surface exchange, improving ORR activity. The DFT results show that the introduction of nickel lowers E_{vo}. Reduced E_{vo} leads to an increase in the oxygen vacancy content of the cathode. After Ni doping PBFM, the TGA result exhibits that weight loss increases, which means more oxygen vacancies. This is also confirmed by XPS analysis. As a descriptor for ORR activity, O p-band center of PBFMN is higher than that of PBFM. This result also demonstrates that PBFMN has higher ORR activity than the non-doped one. The oxygen adsorption energy is calculated to investigate the role of NiO on ORR. The energy required for oxygen to adsorb onto the surface of nickel oxide is lower than that on the PBFM and PBFMN. The lower energy means that oxygen tends to adsorb on NiO surface rather than to the perovskite surface. The adsorption energy on the NiO and PBFM surface is negative, which means it is spontaneous thermodynamically. In addition, the O–O bond length is 1.53, 1.25 and 1.24 Å when O_2 adsorbed on NiO, PBFM and PBFMN respectively. The larger bond length is beneficial for breaking the O–O bond [44,45]. Therefore, NiO enhances the oxygen adsorption and dissociation, thus improves

ORR kinetics.

In addition, proton transfer and hydration ability are also essential for cathode reaction. The proton formation mechanism is described as

$$V_O^{\cdot\cdot} + H_2O + O_O^{\times} \rightarrow 2OH_O \qquad (5)$$

The oxygen vacancy is taken as a prerequisite for proton formation [46,47]. High concentration of oxygen vacancy contributes to proton transfer. The DFT calculation shows that the proton transfer energy barrier of PBFMN is lower than PBFM. Moreover, proton formation requires the presence of water molecules. E_h for PBFM is much higher than that for PBFMN, which means that hydration reactions of PBFMN are easier than PBFM. The electrode process is analyzed with DRT curves of single cell. The strong peak in P2 corresponds to the proton transfer at the cathode. Compared to PBFM, the PBFMN exhibits lower intensity in P2, which means that PBFMN with NiO nanoparticles has high proton conductivity. The peak intensity in the P1 of PBFMN is decreased, which is related to oxygen adsorption and dissociation [48]. These results indicate that the oxygen adsorption and dissociation is enhanced. Based on the DRT of symmetrical cells, PBFMN significantly decrease the polarization in the entire frequency range by enhancing oxygen reduction and charge transfer of ORR.

Combined with the DFT simulations and DRT analysis above, the enhanced reaction mechanism on the surface of PBFMN is proposed (Fig. 6). Oxygen is initially adsorbed on surface. The oxygen molecules
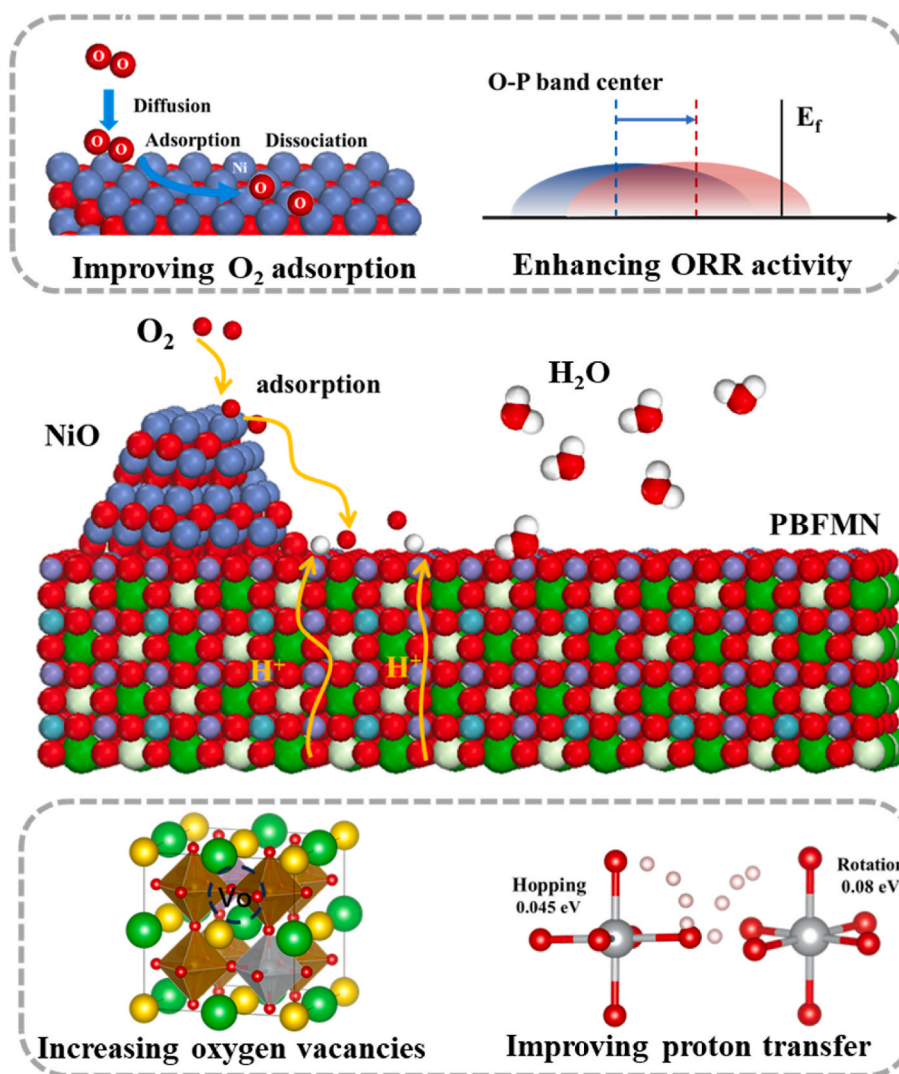

Fig. 6. Reaction mechanism and advantages of PBFMN.

then dissociate and spillover on the perovskite surface through direct combination with the oxygen vacancies. Meanwhile, protons transfer to triple three-phase boundary through PBFMN perovskite phase and then react with adsorbed O to form water. The NiO phase improve oxygen adsorption and surface exchange. The substitution of Ni for Fe in PBFM increases oxygen vacancies, thus enhancing ORR kinetics and proton transfer. PBFMN possesses a high triple-conducting ($e^-/O^{2-}/H^+$) ability, which extends reaction sites to the entire cathode surface.

4.2. Performance and stability analysis

PBFMN with triple conduction capability enhances ORR kinetics, improving PCFC performance. The performance of a single cell with PBFMN presents a P_{max} of 1.23 W cm^{-2} and a low R_P of 0.05 Ω cm^2. Durability is another important index for evaluating cathode. At a discharging current at 1A cm^{-2}, no evident performance degradation is observed. These means that PBFMN cathode has a good durability in PCFC.

5. Conclusions

In summary, we prepared a dual modified PBFMN cathode in a PCFC. The results of XRD and TEM confirm that PBFMN composes of a major perovskite and a minor NiO phases. Ni-doped PBFM increases oxygen vacancy concentration according to the results of TGA and XPS. Based on symmetric cells and DFT simulations, Ni-doped PBFM with NiO nanoparticles improves oxygen adsorption and surface exchange. The ORR kinetics and proton transfer are enhanced when Ni is doped into PBFM. Due to synergistic effects of perovskite and NiO nanoparticles, the single cell with PBFMN exhibits a high peak power density of 1.23 W cm^{-2} and a lower R_P of 0.05 Ω cm^2 at 700 °C. The stable performance of a single cell with PBFMN cathode is maintained over 200 h without obvious degradation. It is one of the best performances among the cobalt-free cathode reported so far. This work is of great importance to rational design of high activity, stable PCFC cathodes.

CRediT authorship contribution statement

Penghui Yao: Writing – original draft, Methodology, Investigation, Formal analysis. **Jian Zhang:** Methodology, Investigation, Conceptualization. **Qianyuan Qiu:** Validation, Investigation, Conceptualization. **Yicheng Zhao:** Validation, Resources, Investigation. **Fangyong Yu:** Validation, Methodology, Conceptualization. **Yongdan Li:** Writing – review & editing, Validation, Supervision, Resources, Conceptualization.

Declaration of competing interest

The authors declare that they have no known competing financial interests or personal relationships that could have appeared to influence the work reported in this paper.

Data availability

Data will be made available on request.

Acknowledgement

References

[1] A.B. Stambouli, E. Traversa, Solid oxide fuel cells (SOFCs): a review of an environmentally clean and efficient source of energy, Renewable Sustainable Energy Rev. 6 (5) (2002) 433–455, https://doi.org/10.1016/S1364-0321(02)00014-X.

[2] J. Zhang, S. Ricote, P.V. Hendriksen, Y. Chen, Advanced materials for thin-film solid oxide fuel cells: recent progress and challenges in boosting the device performance at low temperatures, Adv. Funct. Mater. 32 (22) (2022) 2111205, https://doi.org/10.1002/adfm.202111205.

[3] D. Zou, Y. Yi, Y. Song, D. Guan, M. Xu, R. Ran, W. Wang, W. Zhou, Z. Shao, The BaCe0.16Y0.04Fe0.8O3−δ nanocomposite: a new high-performance cobalt-free triple-conducting cathode for protonic ceramic fuel cells operating at reduced temperatures, J. Mater. Chem. A 10 (10) (2022) 5381–5390, https://doi.org/10.1039/D1TA10652J.

[4] J. Kim, A. Jun, O. Gwon, S. Yoo, M. Liu, J. Shin, T.-H. Lim, G. Kim, Hybrid-solid oxide electrolysis cell: a new strategy for efficient hydrogen production, Nano Energy 44 (2018) 121–126, https://doi.org/10.1016/j.nanoen.2017.11.074.

[5] G. Yang, C. Su, H. Shi, Y. Zhu, Y. Song, W. Zhou, Z. Shao, Toward reducing the operation temperature of solid oxide fuel cells: our past 15 Years of efforts in cathode development, Energy Fuel 34 (12) (2020) 15169–15194, https://doi.org/10.1021/acs.energyfuels.0c01887.

[6] Z. Yang, J. Zhang, B. Wu, X. Zhao, X. Lu, Y. Zhao, Y. Li, Self-assembled La0.6Sr0.4FeO3−δ-La1.2Sr0.8NiO4+δ composite cathode for protonic ceramic fuel cells, Ceram. Int. 49 (15) (2023) 25381–25388, https://doi.org/10.1016/j.ceramint.2023.05.074.

[7] X. Zhou, N. Hou, T. Gan, L. Fan, Y. Zhang, J. Li, G. Gao, Y. Zhao, Y. Li, Enhanced oxygen reduction reaction activity of BaCe0.2Fe0.8O3-δ cathode for proton-conducting solid oxide fuel cells via Pr-doping, J. Power Sources 495 (2021) 229776, https://doi.org/10.1016/j.jpowsour.2021.229776.

[8] X. Lv, H. Chen, W. Zhou, S.-D. Li, Z. Shao, A CO2-tolerant SrCo0.8Fe0.15Zr0.05O3−δ cathode for proton-conducting solid oxide fuel cells, J. Mater. Chem. A 8 (22) (2020) 11292–11301, https://doi.org/10.1039/D0TA02435J.

[9] R. Zohourian, R. Merkle, G. Raimondi, J. Maier, Mixed-conducting perovskites as cathode materials for protonic ceramic fuel cells: understanding the trends in proton uptake, Adv. Funct. Mater. 28 (35) (2018) 1801241, https://doi.org/10.1002/adfm.201801241.

[10] Y. Song, Y. Chen, W. Wang, C. Zhou, Y. Zhong, G. Yang, W. Zhou, M. Liu, Z. Shao, Self-Assembled triple-conducting nanocomposite as a superior protonic ceramic fuel cell cathode, Joule 3 (11) (2019) 2842–2853, https://doi.org/10.1016/j.joule.2019.07.004.

[11] X. Xu, H. Wang, M. Fronzi, X. Wang, L. Bi, E. Traversa, Tailoring cations in a perovskite cathode for proton-conducting solid oxide fuel cells with high performance, J. Mater. Chem. A 7 (36) (2019) 20624–20632, https://doi.org/10.1039/C9TA05300J.

[12] B. Lin, H. Ding, Y. Dong, S. Wang, X. Zhang, D. Fang, G. Meng, Intermediate-to-low temperature protonic ceramic membrane fuel cells with Ba0.5Sr0.5Co0.8Fe0.2O3−δ–BaZr0.1Ce0.7Y0.2O3−δ composite cathode, J. Power Sources 186 (1) (2009) 58–61, https://doi.org/10.1016/j.jpowsour.2008.09.041.

[13] W. Bian, W. Wu, B. Wang, W. Tang, M. Zhou, C. Jin, H. Ding, W. Fan, Y. Dong, J. Li, D. Ding, Revitalizing interface in protonic ceramic cells by acid etch, Nature 604 (7906) (2022) 479–485, https://doi.org/10.1038/s41586-022-04457-y.

[14] A. Seong, J. Kim, D. Jeong, S. Sengodan, M. Liu, S. Choi, G. Kim, Electrokinetic Proton Transport in Triple (H+/O2−/e−) Conducting Oxides as a Key Descriptor for Highly Efficient Protonic Ceramic Fuel Cells, Adv. Sci. 8 (11) (2021) 2004099, https://doi.org/10.1002/advs.202004099.

[15] X. Xu, Y. Xu, J. Ma, Y. Yin, M. Fronzi, X. Wang, L. Bi, Tailoring electronic structure of perovskite cathode for proton-conducting solid oxide fuel cells with high performance, J. Power Sources 489 (2021) 229486, https://doi.org/10.1016/j.jpowsour.2021.229486.

[16] H. Tong, W. Hu, M. Fu, C. Yang, Z. Tao, Nickel-regulated composite cathode with balanced triple conductivity for proton-conducting solid oxide fuel cells, Adv. Sci. 10 (36) (2023) 2304555, https://doi.org/10.1002/advs.202304555.

[17] H. Tong, M. Fu, Y. Yang, F. Chen, Z. Tao, A novel self-assembled cobalt-free perovskite composite cathode with triple-conduction for intermediate proton-conducting solid oxide fuel cells, Adv. Funct. Mater. 32 (48) (2022) 2209695, https://doi.org/10.1002/adfm.202209695.

[18] N. Wang, S. Hinokuma, T. Ina, C. Zhu, H. Habazaki, Y. Aoki, Mixed proton–electron–oxide ion triple conducting manganite as an efficient cobalt-free cathode for protonic ceramic fuel cells, J. Mater. Chem. A 8 (21) (2020) 11043–11055, https://doi.org/10.1039/D0TA03899G.

[19] J. Zhou, L. Xu, C. Ding, C. Wei, Z. Tao, Layered perovskite (PrBa)0.95(Fe0.9Mo0.1)2O5+δ as electrode materials for high-performing symmetrical solid oxide electrolysis cells, Mater. Lett. 257 (2019) 126758, https://doi.org/10.1016/j.matlet.2019.126758.

[20] D. Kim, S.J. Son, M. Kim, H.J. Park, J.H. Joo, PrBaFe2O5+δ promising electrode for redox-stable symmetrical proton-conducting solid oxide fuel cells, J. Eur. Ceram. Soc. 41 (12) (2021) 5939–5946, https://doi.org/10.1016/j.jeurceramsoc.2021.05.031.

[21] M. Liang, Y. Zhu, Y. Song, D. Guan, Z. Luo, G. Yang, S.P. Jiang, W. Zhou, R. Ran, Z. Shao, A new durable surface nanoparticles-modified perovskite cathode for protonic ceramic fuel cells from selective cation exsolution under oxidizing atmosphere, Adv. Mater. 34 (10) (2022) 2106379, https://doi.org/10.1002/adma.202106379.

[22] H. Zhang, K. Xu, F. He, Y. Zhou, K. Sasaki, B. Zhao, Y. Choi, M. Liu, Y. Chen, Surface regulating of a double-perovskite electrode for protonic ceramic fuel cells

to enhance oxygen reduction activity and contaminants poisoning tolerance, Adv. Energy Mater. 12 (26) (2022) 2200761, https://doi.org/10.1002/aenm.202200761.

[23] J. Jing, Z. Lei, C. Wang, Z. Zheng, H. Wang, P. Zhang, Z. Yang, S. Peng, Boosting performance of a protonic ceramic fuel cell by the incorporation of active nano-structured layers, ACS Sustainable Chem. Eng. 11 (28) (2023) 10303–10310, https://doi.org/10.1021/acssuschemeng.3c00706.

[24] M. Liang, Y. Wang, Y. Song, D. Guan, J. Wu, P. Chen, A. Maradesa, M. Xu, G. Yang, W. Zhou, W. Wang, R. Ran, F. Ciucci, Z. Shao, High-temperature water oxidation activity of a perovskite-based nanocomposite towards application as air electrode in reversible protonic ceramic cells, Appl. Catal., B 331 (2023) 122682, https://doi.org/10.1016/j.apcatb.2023.122682.

[25] K. Okhotnikov, T. Charpentier, S. Cadars, Supercell program: a combinatorial structure-generation approach for the local-level modeling of atomic substitutions and partial occupancies in crystals, J. Cheminf. 8 (1) (2016) 17, https://doi.org/10.1186/s13321-016-0129-3.

[26] T. Zhu, H.E. Troiani, L.V. Mogni, M. Han, S.A. Barnett, Ni-substituted $Sr(Ti,Fe)O_3$ SOFC anodes: achieving high performance via metal alloy nanoparticle exsolution, Joule 2 (3) (2018) 478–496, https://doi.org/10.1016/j.joule.2018.02.006.

[27] S. Liu, K.T. Chuang, J.-L. Luo, Double-layered perovskite anode with in situ exsolution of a Co–Fe alloy to cogenerate ethylene and electricity in a proton-conducting ethane fuel cell, ACS Catal. 6 (2) (2016) 760–768, https://doi.org/10.1021/acscatal.5b02296.

[28] T. Gan, H. Song, X. Fan, Y. Liu, S. Liu, Y. Zhao, Y. Li, A rational design of highly active and coke-resistant anode for methanol-fueled solid oxide fuel cells with Sn doped $Ni-Ce_{0.8}Sm_{0.2}O_{2-\delta}$, Chem. Eng. J. 455 (2023) 140692 https://doi.org/10.1016/j.cej.2022.140692.

[29] N. Hou, T. Yao, P. Li, X. Yao, T. Gan, L. Fan, J. Wang, X. Zhi, Y. Zhao, Y. Li, A-site ordered double perovskite with in situ exsolved core–shell nanoparticles as anode for solid oxide fuel cells, ACS Appl. Mater. Interfaces 11 (7) (2019) 6995–7005, https://doi.org/10.1021/acsami.8b19928.

[30] M. Zhou, Z. Liu, M. Chen, Z. Zhu, D. Cao, J. Liu, Electrochemical performance and chemical stability of proton-conducting $BaZr_{0.8-x}Ce_xY_{0.2}O_{3-\delta}$ electrolytes, J. Am. Ceram. Soc. 105 (9) (2022) 5711–5724, https://doi.org/10.1111/jace.18500.

[31] J. Li, L. Fan, N. Hou, Y. Zhao, Y. Li, Solid oxide fuel cell with a spin-coated yttria stabilized zirconia/gadolinia doped ceria bi-layer electrolyte, RSC Adv. 12 (21) (2022) 13220–13227, https://doi.org/10.1039/D2RA02035A.

[32] P. Yao, J. Zhang, Q. Qiu, G. Li, Y. Zhao, F. Yu, Y. Li, Design of a perovskite oxide cathode for a protonic ceramic fuel cell, Ceram. Int. (2023), https://doi.org/10.1016/j.ceramint.2023.11.015.

[33] Y. Chen, S. Yoo, W. Zhang, J.H. Kim, Y. Zhou, K. Pei, N. Kane, B. Zhao, R. Murphy, Y. Choi, M. Liu, Effective promotion of oxygen reduction reaction by in situ formation of nanostructured catalyst, ACS Catal. 9 (8) (2019) 7137–7142, https://doi.org/10.1021/acscatal.9b01738.

[34] J. Jing, Z. Lei, Z. Zheng, H. Wang, P. Zhang, Z. Wang, H. Xu, Z. Yang, Triple conducting perovskite $Ba_{0.95}La_{0.05}Fe_{0.8}Zn_{0.2}O_{3-\delta}$ as oxygen electrode for reversible protonic ceramic cells, Int. J. Hydrogen Energy 48 (24) (2023) 9037–9045, https://doi.org/10.1016/j.ijhydene.2022.12.019.

[35] J. Wang, Z. Li, H. Zang, Y. Sun, Y. Zhao, Z. Wang, Z. Zhu, Z. Wei, Q. Zheng, $BaZr_{0.1}Fe_{0.9-x}Ni_xO_{3-\delta}$ cubic perovskite oxides for protonic ceramic fuel cell

[36] J. Ma, Y. Pan, Y. Wang, Y. Chen, A Sr and Ni doped Ruddlesden−Popper perovskite oxide $La_{1.6}Sr_{0.4}Cu_{0.6}Ni_{0.4}O_{4+\delta}$ as a promising cathode for protonic ceramic fuel cells, J. Power Sources 509 (2021) 230369, https://doi.org/10.1016/j.jpowsour.2021.230369.

cathodes, Int. J. Hydrogen Energy 47 (15) (2022) 9395–9407, https://doi.org/10.1016/j.ijhydene.2022.01.012.

[37] L. Miao, J. Hou, Z. Gong, Z. Jin, W. Liu, A high-performance cobalt-free Ruddlesden-Popper phase cathode $La_{1.2}Sr_{0.8}Ni_{0.6}Fe_{0.4}O_{4+\delta}$ for low temperature proton-conducting solid oxide fuel cells, Int. J. Hydrogen Energy 44 (14) (2019) 7531–7537, https://doi.org/10.1016/j.ijhydene.2019.01.255.

[38] J. Cui, J. Wang, X. Zhang, G. Li, K. Wu, Y. Cheng, J. Zhou, Low thermal expansion material $Bi_{0.5}Ba_{0.5}FeO_{3-\delta}$ in application for proton-conducting ceramic fuel cells cathode, Int. J. Hydrogen Energy 44 (38) (2019) 21127–21135, https://doi.org/10.1016/j.ijhydene.2019.02.127.

[39] B. Liu, Z. Li, X. Yang, D. Yan, J. Li, L. Jia, Novel mixed H+/e−/O2− conducting cathode material $PrBa_{0.9}K_{0.1}Fe_{1.9}Zn_{0.1}O_{5+\delta}$ for proton-conducting solid oxide fuel cells, J. Mater. Chem. A 10 (34) (2022) 17425–17433, https://doi.org/10.1039/D2TA04457A.

[40] S.M. Choi, H. An, K.J. Yoon, B.-K. Kim, H.-W. Lee, J.-W. Son, H. Kim, D. Shin, H.-I. Ji, J.-H. Lee, Electrochemical analysis of high-performance protonic ceramic fuel cells based on a columnar-structured thin electrolyte, Appl. Energy 233–234 (2019) 29–36, https://doi.org/10.1016/j.apenergy.2018.10.043.

[41] Y. Chen, Y. Choi, S. Yoo, Y. Ding, R. Yan, K. Pei, C. Qu, L. Zhang, I. Chang, B. Zhao, Y. Zhang, H. Chen, Y. Chen, C. Yang, B. deGlee, R. Murphy, J. Liu, M. Liu, A highly efficient multi-phase catalyst dramatically enhances the rate of oxygen reduction, Joule 2 (5) (2018) 938–949, https://doi.org/10.1016/j.joule.2018.02.008.

[42] K. Xu, H. Zhang, Y. Xu, F. He, Y. Zhou, Y. Pan, J. Ma, B. Zhao, W. Yuan, Y. Chen, M. Liu, An efficient steam-induced heterostructured air electrode for protonic ceramic electrochemical cells, Adv. Funct. Mater. 32 (23) (2022) 2110998, https://doi.org/10.1002/adfm.202110998.

[43] N. Mushtaq, Y. Lu, C. Xia, W. Dong, B. Wang, X. Wang, M.A.K. Yousaf Shah, S. Rauf, N. Jingjing, E. Hu, H. Xiao, R. Raza, J.-S. Kim, B. Zhu, Design principle and assessing the correlations in Sb-doped $Ba_{0.5}Sr_{0.5}FeO_{3-\delta}$ perovskite oxide for enhanced oxygen reduction catalytic performance, J. Catal. 395 (2021) 168–177, https://doi.org/10.1016/j.jcat.2020.12.005.

[44] H. Dai, Y. Yin, X. Li, C. Ma, Z. Chen, M. Hua, L. Bi, A new Sc-doped $La_{0.5}Sr_{0.5}MnO_{3-\delta}$ cathode allows high performance for proton-conducting solid oxide fuel cells, Sustainable Mater, Technol. 32 (2022) e00409, https://doi.org/10.1016/j.susmat.2022.e00409.

[45] J.B. Goodenough, Y. Kim, Challenges for rechargeable batteries, J. Power Sources 196 (16) (2011) 6688–6694, https://doi.org/10.1016/j.jpowsour.2010.11.074.

[46] Z. Tao, L. Yan, J. Qiao, B. Wang, L. Zhang, J. Zhang, A review of advanced proton-conducting materials for hydrogen separation, Prog. Mater. Sci. 74 (2015) 1–50, https://doi.org/10.1016/j.pmatsci.2015.04.002.

[47] I.T. Bello, S. Zhai, Q. He, C. Cheng, Y. Dai, B. Chen, Y. Zhang, M. Ni, Materials development and prospective for protonic ceramic fuel cells, Int. J. Energy Res. 46 (3) (2022) 2212–2240, https://doi.org/10.1002/er.7371.

[48] H. Shi, C. Su, X. Xu, Y. Pan, G. Yang, R. Ran, Z. Shao, Building ruddlesden–popper and single perovskite nanocomposites: a new strategy to develop high-performance cathode for protonic ceramic fuel cells, Small 17 (35) (2021) 2101872, https://doi.org/10.1002/smll.202101872.